2006

Sptizer and JCMT Observations of the Active Galactic Nucleus in the Sombrero Galaxy (NGC 4594)

G. J. Bendo
B. A. Buckalew
D. A. Dale
B. T. Draine
R. D. Joseph, et al.

SPITZER AND JCMT OBSERVATIONS OF THE ACTIVE GALACTIC NUCLEUS IN THE SOMBRERO GALAXY (NGC 4594)

George J. Bendo,[1,2] Brent A. Buckalew,[3] Daniel A. Dale,[4] Bruce T. Draine,[5] Robert D. Joseph,[6]
Robert C. Kennicutt, Jr.,[2,7] Kartik Sheth,[3] John-David T. Smith,[2] Fabian Walter,[8]
Daniela Calzetti,[9] John M. Cannon,[8] Charles W. Engelbracht,[2] Karl D. Gordon,[2]
George Helou,[3] David Hollenbach,[10] Eric J. Murphy,[11] and Hélène Roussel[8]

ABSTRACT

We present *Spitzer* 3.6–160 μm images, *Spitzer* mid-infrared spectra, and JCMT SCUBA 850 μm images of the Sombrero Galaxy (NGC 4594), an Sa galaxy with a $10^9 \, M_\odot$ low-luminosity active galactic nucleus (AGN). The brightest infrared sources in the galaxy are the nucleus and the dust ring. The spectral energy distribution of the AGN demonstrates that, while the environment around the AGN is a prominent source of mid-infrared emission, it is a relatively weak source of far-infrared emission, as had been inferred for AGNs in previous research. The weak nuclear 160 μm emission and the negligible polycyclic aromatic hydrocarbon emission from the nucleus also implies that the nucleus is a site of only weak star formation activity and the nucleus contains relatively little cool interstellar gas needed to fuel such activity. We propose that this galaxy may be representative of a subset of low-ionization nuclear emission region galaxies that are in a quiescent AGN phase because of the lack of gas needed to fuel circumnuclear star formation and Seyfert-like AGN activity. Surprisingly, the AGN is the predominant source of 850 μm emission. We examine the possible emission mechanisms that could give rise to the 850 μm emission and find that neither thermal dust emission, CO line emission, bremsstrahlung emission, nor the synchrotron emission observed at radio wavelengths can adequately explain the measured 850 μm flux density by themselves. The remaining possibilities for the source of the 850 μm emission include a combination of known emission mechanisms, synchrotron emission that is self-absorbed at wavelengths longer than 850 μm, or unidentified spectral lines in the 850 μm band.

Subject headings: galaxies: active — galaxies: individual (NGC 4594) — galaxies: ISM — galaxies: nuclei — infrared: galaxies

Online material: color figures

1. INTRODUCTION

A key yet simple point in understanding the infrared spectral energy distributions (SEDs) of galaxies is separating the component of the dust emission that is primarily heated by an active galactic nucleus (AGN) from the component that is primarily heated by star formation. Such simple knowledge is vital for examining the connection between starbursts and AGNs, particularly those that are dust-enshrouded; for modeling the SEDs of dust emission from galaxies; for validating or modifying the unified model of AGNs; and for understanding distant, unresolved AGNs. This issue is especially important in debates on the origins of far-infrared emission in powerful AGNs such as quasi-stellar objects (see Genzel & Cesarsky 2000 for a discussion).

Results from the *Infrared Astronomical Satellite* (*IRAS*) have shown that the 60/25 μm flux ratios of Seyfert galaxies and other AGNs were lower than for starbursts and other spiral galaxies (e.g., de Grijp et al. 1985, 1987; Osterbrock & de Roberts 1985; Kailey & Lebofsky 1988; Rodriguez Espinosa et al. 1987; Rowan-Robinson & Crawford 1989). The enhancement in the 25 μm emission was interpreted as originating from the environment of the AGN, whereas the 60 and 100 μm emission was interpreted as originating from star formation activity. However, since both the AGN and star formation were cospatial, disentangling the infrared SEDs of both has proved to be difficult.

A few studies that either combined ground-based mid-infrared and *IRAS* data (e.g., Maiolino et al. 1995) or used *Infrared Space Observatory* data (e.g., Rodriguez Espinosa & Perez Garcia 1997; Perez Garcia et al. 1998, 2000) began to separate the infrared emission from AGNs and star formation in nearby galaxies. Most of the evidence suggesting that the far-infrared emission is related to star formation rather than AGN activity relies on the similarities between the far-infrared SEDs of Seyfert and non-Seyfert galaxies, on the consistency of the far-infrared SEDs in a broad range of Seyfert galaxies, and on the relation between far-infrared emission and stellar emission. While these results are good evidence for the far-infrared emission of Seyfert galaxies originating from circumnuclear star formation, the results are only inferences.

Generally, it is very challenging to separate the infrared emission from dust heated by an AGN and the infrared emission from dust heated by circumnuclear star formation. The problem lies not

[1] Astrophysics Group, Imperial College, Blackett Laboratory, Prince Consort Road, London SW7 2AZ, UK; g.bendo@imperial.ac.uk.
[2] Steward Observatory, University of Arizona, 933 North Cherry Avenue, Tucson, AZ 85721.
[3] California Institute of Technology, MC 314-6, Pasadena, CA 91101.
[4] Department of Physics and Astronomy, University of Wyoming, Laramie, WY 82071.
[5] Princeton University Observatory, Peyton Hall, Princeton, NJ 08544-1001.
[6] Institute for Astronomy, University of Hawaii, 2680 Woodlawn Drive, Honolulu, HI 96822.
[7] Institute of Astronomy, University of Cambridge, Cambridge CB3 0HA, UK.
[8] Max-Planck-Institut für Astronomie, Königstuhl 17, D-69117 Heidelberg, Germany.
[9] Space Telescope Science Institute, 3700 San Martin Drive, Baltimore, MD 21218.
[10] NASA Ames Research Center, MS 245-3, Moffett Field, CA 94035-1000.
[11] Department of Astronomy, Yale University, P.O. Box 208101, New Haven, CT 06520.

only with the limited resolution of previous instrumentation. The major problem is that many nearby Seyfert galaxies have circumnuclear star formation that will produce centralized dust emission that is difficult to disentangle from far-infrared emission from dust heated by the AGN. Both sources of emission are effectively superimposed.

The Sombrero Galaxy (NGC 4954), at a distance of 9.2 Mpc (the average of measurements from Ford et al. 1996 and Ajhar et al. 1997), is ideal for studying the separate SEDs of dust heated by the AGN and dust heated by starlight. The galaxy's nucleus is classified in Ho et al. (1997) as a low-ionization nuclear emission region (LINER). It does contain a supermassive black hole with a mass of $10^9 M_\odot$ (Kormendy et al. 1996), and the AGN is detected as a point source in hard X-ray (e.g., Pellegrini et al. 2002, 2003) and radio (e.g., Hummel et al. 1984) emission. What makes this particular LINER unique is that the geometry of the mid- and far-infrared dust emission is relatively easy to model, and the dust that is primarily heated by star formation is mostly concentrated in a ring relatively far from the AGN, as we demonstrate in this paper. Therefore, the SED of the dust heated by the AGN can be separated from the SED of the diffuse interstellar dust. This galaxy has been studied in the infrared/submillimeter wave band in previous works (e.g., Rice et al. 1988; Schmitt et al. 1997; Krause et al. 2006), but these studies were limited by the resolution of the *IRAS* data and could only examine the global SED in the far-infrared.

In this paper we present *Spitzer Space Telescope* (Werner et al. 2004) Infrared Array Camera (IRAC; Fazio et al. 2004) 3.6–8.0 μm images, Multiband Imaging Photometer for *Spitzer* (MIPS; Rieke et al. 2004) 24–160 μm images, and Infrared Spectrograph (IRS; Houck et al. 2004) mid-infrared spectra, as well as James Clerk Maxwell Telescope (JCMT) Submillimeter Common-User Bolometer Array (SCUBA; Holland et al. 1999) 850 μm images of the Sombrero Galaxy that we use to examine the separate SEDs of the AGN and the dust ring. In § 2 we describe the observations and data reductions. In § 3.1 we discuss the images qualitatively. In § 3.2 we briefly discuss the IRS mid-infrared spectra. In § 3.3 we model the images of the galaxy in each wave band to determine SEDs for global emission and for the separate physical components of the galaxy. Then, in § 4 we discuss the major results from the SED of the AGN.

2. OBSERVATIONS AND DATA REDUCTION

2.1. 3.6–8.0 μm *Images*

The 3.6–8.0 μm data were taken with IRAC on the *Spitzer Space Telescope* on 2004 June 10 in IRAC campaign 9 and on 2005 January 22 in IRAC campaign 18 as part of the *Spitzer* Infrared Nearby Galaxies Survey (SINGS; Kennicutt et al. 2003). The observations consist of a series of $5' \times 5'$ individual frames that are offset $2.'5$ from each other. The two separate sets of observations allow asteroids to be recognized and provide observations at orientations up to a few degrees apart to ease removal of detector artifacts. Points in the center are imaged 8 times in 30 s exposures. The FWHM of the point-spread functions (PSFs) are $1.''6$–$1.''9$ for the four wave bands.

The data are processed using a special SINGS IRAC pipeline. First, a geometric distortion correction is applied to the individual frames. Data from the second set of observations are rotated to the same orientation as the first set of observations. Bias levels are subtracted from the 5.7 μm data by subtracting a bias frame (made by combining all data frames for the observations) from each frame. Next, the image offsets are determined through image cross-correlation. Following this, bias drift is removed. Finally, cosmic-ray masks are created using standard drizzle methods, and

final image mosaics are created using a drizzle technique. The final pixel scales are set at $\sim 0.''75$. A final background is measured in small regions outside the target that are free of bright foreground/background sources, and then this final background is subtracted from the data. The contribution of uncertainties in the background (both in terms of the statistical fluctuations of the pixels and the uncertainty in the mean background subtracted from the data) to uncertainties in the integrated global flux densities is less than 0.1%. The dominant source of uncertainty is the 30% uncertainty in the calibration factor (including the uncertainty in the extended source calibration) applied to the final mosaics.

2.2. 24–160 μm *Images*

The 24, 70, and 160 μm data were taken with MIPS on the *Spitzer Space Telescope* on 2004 July 10 and 12 in MIPS campaign 10 as part of the SINGS survey. The observations were obtained using the scan-mapping mode in two separate visits to the galaxy. Two separate sets of observations separated by more than 24 hr allow asteroids to be recognized and provide observations at orientations up to a few degrees apart to ease removal of detector artifacts. As a result of redundancy inherent in the scan-mapping mode, each pixel in the core map area was effectively observed 40, 20, and 4 times at 24, 70, and 160 μm, respectively, resulting in integration times per pixel of 160, 80, and 16 s, respectively. The FWHM of the PSFs of the 24, 70, and 160 μm data are $6''$, $15''$, and $40''$, respectively.

The MIPS data were processed using the MIPS Data Analysis Tools version 2.80 (Gordon et al. 2005). The processing for the 24 μm data differed notably from the 70 and 160 μm data, so they are discussed separately.

First, the 24 μm images were processed through a droop correction (that removes an excess signal in each pixel that is proportional to the signal in the entire array) and a nonlinearity correction. Following this, the dark current was subtracted. Next, scan-mirror-position–dependent flats and scan-mirror-position–independent flats were applied to the data. Latent images from bright sources, erroneously high or low pixel values, and unusually noisy frames were also masked out. Finally, mosaics of the data from each set of observations were made. In each mosaic, the background was subtracted in two steps. First, to remove the broad zodiacal light emission, a function that varied linearly in the x- and y-directions was fit to the region outside the optical disk in a box 3 times the size of the optical major axis of the galaxy. This plane was then subtracted from the data. Next, to remove residual background emission from cirrus structure near the galaxy, an additional offset measured in multiple small circular regions near the optical disk was subtracted. After this final subtraction, the two mosaics were averaged together to produce the final 24 μm mosaic.

In the 70 and 160 μm data, readout jumps and cosmic-ray hits were first removed from the data. Next, the stim flash frames taken by the instrument were used as responsivity corrections. The dark current was subtracted from the data, an illumination correction was applied, and then short-term variations in signal (i.e., short-term drift) were subtracted from the data. (This last step also subtracts off the background.) Following this, erroneously high or low pixel values were identified statistically or visually and removed from the data. Single 70 and 160 μm mosaics were made from all of the data, and a residual offset measured in two regions to the north and south of the target was subtracted from the final maps.

The background noise is a relatively small contributor (less than 0.1%) to the uncertainties in the integrated global flux densities. The dominant source of uncertainty is the uncertainty in
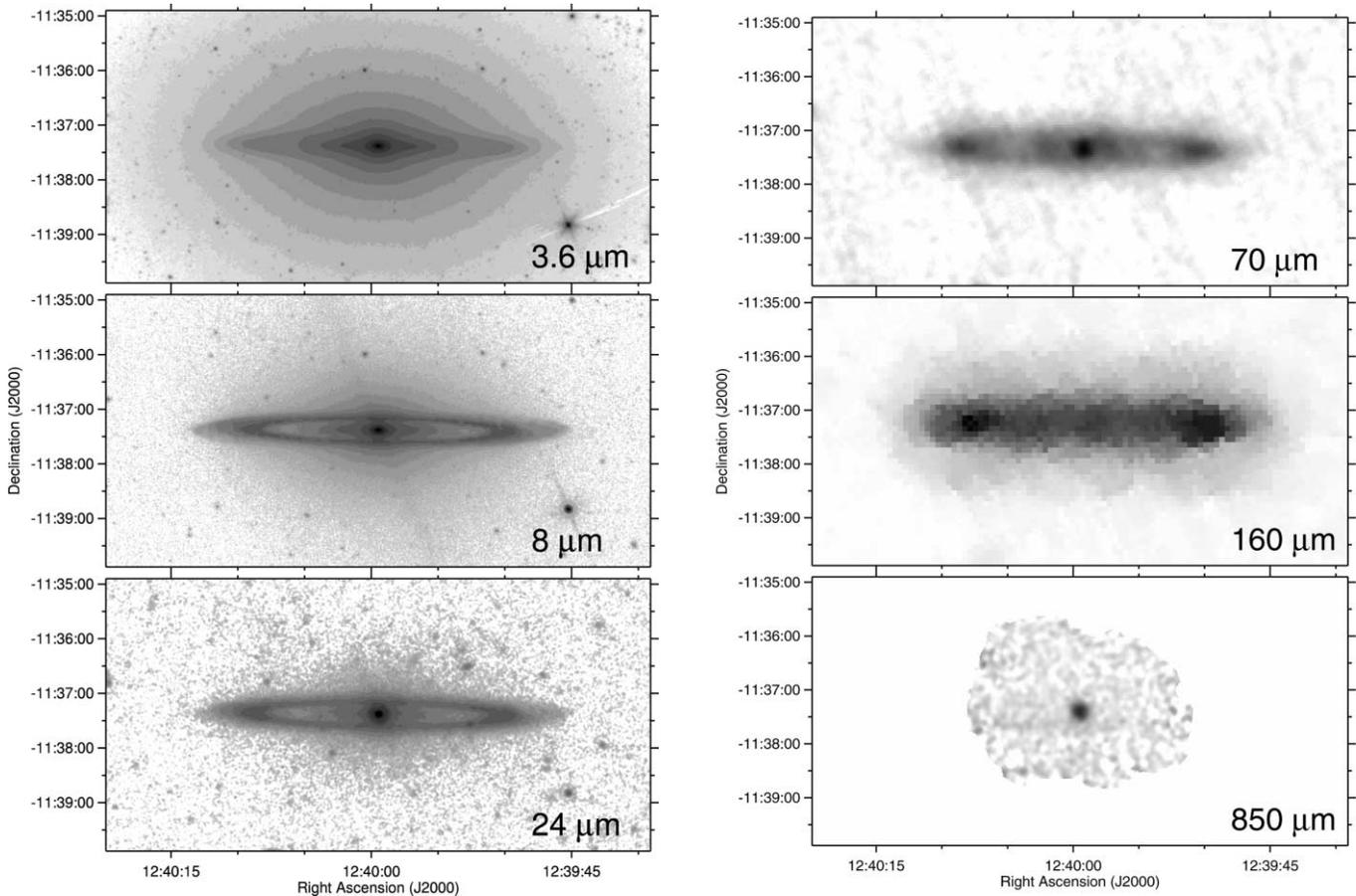
Fig. 1.—Images of NGC 4594 at 3.6, 8, 24, 70, 160, and 850 μm. Each image is $10' \times 5'$, with north up and east to the left. The scaling of the brightness in all images is logarithmic. Note that only the inner $\sim 3' \times \sim 2.'25$ region was covered in the 850 μm band and that the very bright and dark pixels at the edges of this region are an artifact of the data processing. [*See the electronic edition of the Journal for a color version of this figure.*]

the calibration factors applied to the final mosaic, which is 10% at 24 μm and 20% at 70 and 160 μm.

2.3. 850 μm Image

The 850 μm data were taken with SCUBA at the JCMT on UT dates 2004 January 17 and 18. Six maps (each of which were 10 integrations, or 10.7 minutes of on-target integration) were taken in jiggle map mode, with each map covering 2.'3 hexagonal regions. Each map was slightly offset from the others to ensure that no holes in the maps were created by noisy bolometers. The total map effectively covers the inner $3' \times 2.'25$ region of the galaxy, with 60 integrations (64 minutes of on-target integration) of observing time of the galaxy nucleus. The FWHM of the PSF of the 850 μm data is 15''.

The 850 μm data were processed with the SCUBA User Reduction Facility (Jenness & Lightfoot 1998). The data were first flat-fielded and corrected for atmospheric extinction. Noisy bolometers were removed next, followed by spike removal. Then the background signal was subtracted using the signal from several bolometers at the north and south edges of the images. The data were calibrated using observations of the submillimeter standards CRL 618 and IRC +10216 and then regridded onto the sky plane. An additional background subtraction was then performed to remove any residual offset that appears when the bolometer signals are regridded onto the sky plane. The background noise is a relatively small contributor to the uncertainties in the integrated fluxes (approximately 1%). The dominant source of uncertainty is the 10% uncertainty in the calibration factor applied to the final image.

2.4. Mid-Infrared Spectra

The 5–38 μm spectra were taken with IRS on the *Spitzer Space Telescope* on 2004 June 24 and 28 in IRS campaign 9 as part of the SINGS survey. The observations were taken in the spectral mapping mode, in which the slit is moved in a raster pattern to build up a redundantly sampled spectral map of the target region. The observations presented here were made with the short-low (5–15 μm, $R = 50-100$), long-low (14–38 μm, $R = 50-100$), and long-high (20–37 μm, $R = 600$) IRS modules. The observations were made as a series of pointings where the spectrometer's slits were stepped across the center of the galaxy. As a result, the observations produce spectral cubes. The sizes of the observed regions depend primarily on the specific module used for the observation.

S12-processed basic calibrated data were used for this analysis. The data were assembled into three-dimensional spectral cubes using Cubism (see Kennicutt et al. 2003, § 6.2). When the spectral cubes are built, bad pixels are identified and masked out, background subtraction is performed, and flux calibration is applied to the data. The calibration uncertainties are 25%.

3. RESULTS

3.1. *Images of NGC 4594*

Figure 1 shows the 3.6, 8, 24, 70, 160, and 850 μm images of NGC 4594. Throughout these wave bands, the sources of emission consist mainly of a nuclear source, a ring with an approximate semimajor axis of $\sim 140''$ (~ 6.2 kpc), a thin disk inside the

ring composed of stars and dust (referred to as the inner disk in this paper), and a bulge. The relative contributions of each of these components to each wave band vary substantially. Aside from these four components, no other significant sources of emission are visible in the galaxy.

In nearby galaxies, the 3.6 μm band is dominated by stellar emission (e.g., Lu et al. 2003). In NGC 4594, the bulge and the inner disk are the two extended features with the highest surface brightnesses at this wave band. The ring is nearly invisible.

The 8 μm emission from spiral galaxies contains a mixture of polycyclic aromatic hydrocarbon (PAH) emission, hot thermal emission from very small grains, and the Rayleigh-Jeans tail of stellar blackbody emission (e.g., Helou et al. 2000; Lu et al. 2003). In the observations of NGC 4594 in this wave band, the ring is a much more prominent source of emission, which implies that it is a strong source of PAH and hot dust emission. Note that the ring (at this resolution) is relatively featureless; only a few knots of enhanced 8 μm emission are visible in the ring. Small extensions from the ring that resemble spiral arms are just barely visible on the east and west ends of the ring. Emission from the inner disk is still visible in this wave band. The bulge emission, which originates from stars (and possibly from hot dust in the atmospheres of evolved stars), is much weaker than at 3.6 μm.

The 24 μm band mostly traces very small grain emission (e.g., Li & Draine 2001), although it could also include stellar emission or thermal emission from strongly heated large dust grains. In this wave band, the nucleus is a more prominent source of emission than at shorter wavelengths. The ring and the inner disk are also still strong sources of emission. Except for a bright knot in the southwest portion of the ring, the ring contains no notable structures. The bulge almost disappears completely at this wavelength, although faint traces of the emission are still visible to the north and south of the ring.

The 70 μm band is one of two bands used in this paper that primarily traces large grain emission (e.g., Li & Draine 2001). The appearance of the 70 μm image looks similar to the 24 μm image. The nucleus, the inner dust disk, and the ring are all still visible, but the bulge is indistinguishable from the background noise (as is expected, since little cool interstellar dust is associated with the bulges of galaxies).

In the 160 μm band, which also traces large grain emission (e.g., Li & Draine 2001), the ring is the most prominent source. The inner disk is a weak source of emission in this wave band, and it cannot be easily distinguished from the ring. In stark contrast to the 24 and 70 μm images, the nucleus is almost completely invisible. These results suggest that the environment of the active nucleus contains relatively little dust and that the dust that is present is heated very strongly.

Even more surprising than the relatively weak 160 μm emission from the nucleus is the relatively strong emission from the nucleus observed at 850 μm. Typically, the 850 μm emission traces $\sim$20–30 K dust emission related to the 160 μm emission (e.g., Dunne & Eales 2001; Bendo et al. 2003; Regan et al. 2004). If these previous results applied to this galaxy, then the ring would be the strongest feature observed at 850 μm, and the nucleus would be relatively faint. Instead, the nucleus is the only submillimeter source detected above the 3 σ level, which implies that the submillimeter emission arises from some source other than $\sim$20–30 K dust.

To understand these images better, we need to create models of the images that include components for each of the images. The results of fitting the models to the data will include flux densities that can be used to construct SEDs. This is done in § 3.3.
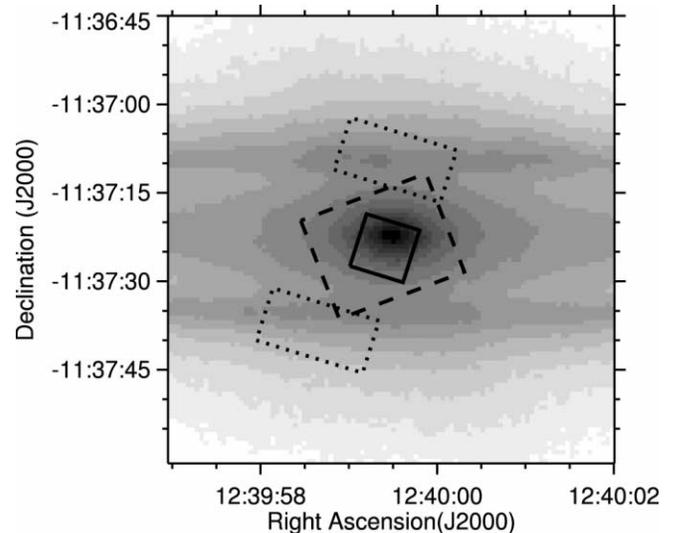

FIG. 2.—Image of the central 75$''$ of NGC 4594 at 8 μm, with boxes showing the regions in which mid-infrared spectra were extracted. The square with the solid line in the center shows where the low-resolution 5–38 μm spectrum for the nucleus was extracted. The dotted rectangles at top and bottom show where the low-resolution 5–38 μm spectrum for the ring was extracted. The dashed rectangle in the center shows where the high-resolution 25–27 μm spectrum for the nucleus was extracted. [See the electronic edition of the Journal for a color version of this figure.]

First, however, we will look at the results from the mid-infrared spectroscopy.

3.2. Mid-Infrared Spectra of the Nucleus and Ring

We can further examine the nature of the nucleus and ring of this galaxy using the IRS spectra. The goal is to understand the primary sources of the dust heating in the nucleus and ring, and specifically to understand whether the dust in the nucleus is heated by star formation or by the AGN. An AGN is clearly present in this galaxy, since a central synchrotron source has been detected in radio (e.g., Hummel et al. 1984) and X-ray (e.g., Pellegrini et al. 2002, 2003) observations and a 10^9 $M_\odot$ central object has been detected through stellar dynamics (Kormendy et al. 1996). The results for this galaxy will reveal whether the AGN is the dominant energy source for the nucleus or whether star formation is a significant factor. These data can also be used as a test of mid-infrared spectral line diagnostics on the spectrum of a known low-luminosity AGN.

The regions in which spectra were extracted are shown in Figure 2. Spectra for individual regions in the galaxy are shown in Figures 3 and 4. Notable features measured in the spectrum of the AGN are listed in Table 1.

The nuclear spectrum is consistent with what is expected from an AGN. Metal lines such as [Ne II], [Ne III], [O IV], and [S III] are present, but PAH features (such as the features at 6.2, 7.7, 11.3, 16.4, and 17.1 μm are weak or absent. Interestingly, some high-excitation lines, notably the [Ne V] line at 14.3 μm, are also absent. This is not surprising, as this is a LINER nucleus with low levels of ionization, although [Ne V] emission often corresponds to AGN activity. The absence of these high-excitation lines in this galaxy's spectrum may have implications for using high-excitation lines as a diagnostic for detecting AGNs in other LINERs. Aside from the absence of high-excitation lines, the spectral lines are consistent with AGN activity. In the diagnostic diagrams of Genzel et al. (1998) and Peeters et al. (2004), the high [O IV]/[Ne II] ratio and the weak 6.2 and 7.7 μm PAH features indicate that this is a
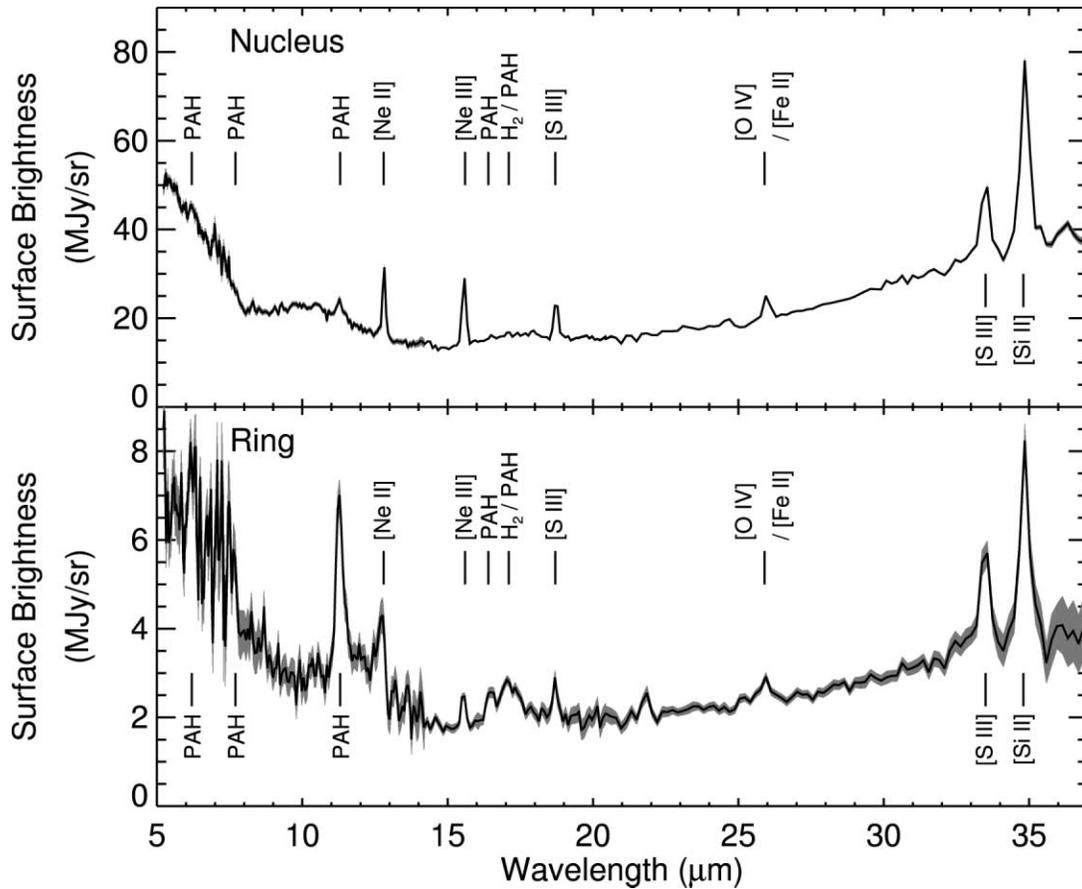
FIG. 3.—Low-resolution IRS spectra of the nucleus and the ring in NGC 4594 at 5–38 μm. The gray regions around the lines represent the uncertainties in the spectra. Major spectral features are identified in the plot. Note the weak or absent PAH features in the nucleus, in contrast to the strong PAH features in the ring. Because of the limitations of the spatial resolution of the telescope, the spectral features longward of 20 μm in the ring spectrum probably include emission from the center. See the text for additional details. See Fig. 4 to see a higher resolution 25.5–26.5 μm spectrum of the nucleus in which the [O IV] and [Fe II] lines are separated.

source dominated by AGN activity. In the alternate diagnostic diagram of Dale et al. (2006), where the 34.8 μm [Si II] is used in place of the 25.9 μm [O IV] line, the nucleus also falls in the AGN-dominated regime.

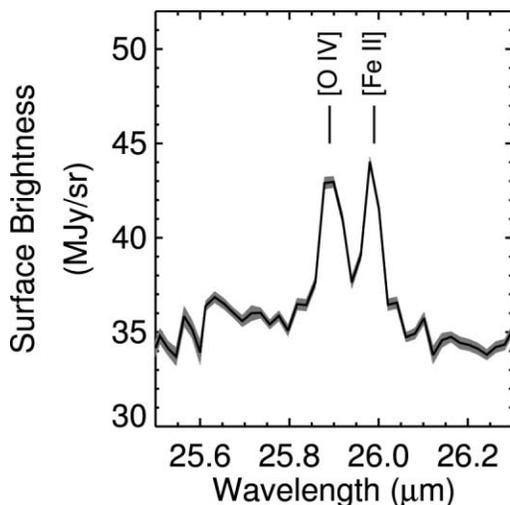The spectrum of the ring is more consistent with star formation activity than the nucleus. PAH emission from the ring, es-

FIG. 4.—High-resolution IRS spectrum of the nucleus in NGC 4594 at 25.5–26.5 μm. The gray regions around the lines represent the uncertainties in the spectra. This plot shows the detail in the [O IV] and [Fe II] line emission.

pecially in the 11.3 μm band, is much stronger. Qualitatively, the stronger PAH features would shift this galaxy into the star formation regime in the diagnostic diagrams of Genzel et al. (1998), Peeters et al. (2004), and Dale et al. (2006). Unfortunately, the observations are too limited to show that the spectrum of the ring is consistent with star formation. The long-high observations, which are needed to measure the 25.9 μm [O IV] line, do not adequately cover the ring. The signal-to-noise ratio is too low for the low-resolution spectrum between 5 and 8 μm for accurate measurement of the 6.2 and 7.7 μm PAH features. Finally, because of the limitations of the spatial resolution, a significant fraction of the flux at wavelengths greater than 20 μm may include emission from the AGN, thus making measurements of the 25.9 μm [O IV] and 34.8 μm [Si II] lines suspect.

Images of the 11.3 μm PAH feature and 25.9 μm [O IV] line emission in Figure 5 bolster these results. These images were

TABLE 1
MEASUREMENT OF SELECT SPECTRAL LINES IN THE NUCLEUS OF NGC 4594

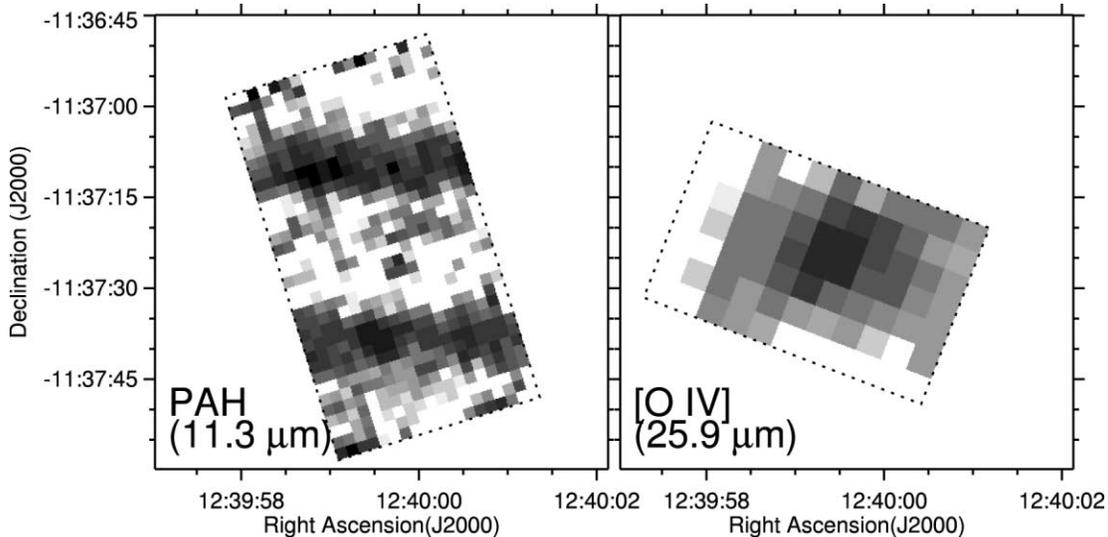| Feature	Measurement
6.2 μm PAH feature equivalent width (μm)	0.0023 ± 0.0004
6.2 μm PAH feature/continuum ratio........................	0.035 ± 0.07
7.7 μm PAH feature equivalent width (μm)	<0.006
7.7 μm PAH feature/continuum ratio........................	<0.04
12.8 μm [Ne II] line strength (ergs cm^{-2} s^{-1})	$(1.86 \pm 0.10) \times 10^{-13}$
25.9 μm [O IV] line strength (ergs cm^{-2} s^{-1})..........	$(5.21 \pm 0.17) \times 10^{-14}$
34.8 μm [Si II] line strength (ergs cm^{-2} s^{-1})	$(7.2 \pm 0.2) \times 10^{-14}$

Fig. 5.—Images of the 11.3 μm PAH feature (*left*) and the 25.9 μm [O IV] line (*right*) for the inner 75″ of NGC 4594. These are images made from the IRS spectral cubes. The dotted lines show the regions covered by the IRS observations. The continuum has been identified and subtracted from the two wave bands on a pixel-by-pixel basis. Note that the PAH emission originates primarily from the ring, whereas the [O IV] emission originates primarily from the nucleus. [*See the electronic edition of the Journal for a color version of this figure.*]

made from the IRS data. To produce the images, the continuum was identified and subtracted on a pixel-by-pixel basis, leaving just the spectral feature emission. In the resulting map for the PAH feature, the emission originates entirely from the ring of the galaxy. Even if PAH emission is treated as only a qualitative tracer of star formation, these results suggest that the star formation is confined to the ring. The [O IV] emission, however, originates mostly from the nucleus. These results from the PAH and [O IV] maps are consistent with the interpretation of an AGN dominating the energetics of the nucleus.

Although generally the absence of nuclear PAH emission implies weak star formation activity (e.g., Genzel et al. 1998; Peeters et al. 2004), PAH emission may be absent in some situations where strong star formation is present. PAH emission is absent in low-metallicity star formation regions (e.g., Engelbracht et al. 2005). This could be an explanation for the absence of PAH emission from the nucleus of NGC 4594. However, since the metallicity of the interstellar medium (ISM) usually peaks in the centers of galaxies and since PAH emission is seen in the ring, the metallicity of the center is probably above the metallicity threshold necessary for PAH emission. PAH emission may also be absent in star formation regions because of the presence of hard radiation fields (e.g., Madden et al. 2006). If this is the case for NGC 4594, the hard radiation field would be from the AGN, which is the dominant source of X-ray photons in the nuclear environment (Pellegrini et al. 2002, 2003). So, even if circum-nuclear star formation is present, the AGN still dominates the interstellar radiation field in the vicinity of the nucleus. Placed in the context of dust heating, the weak nuclear PAH emission indicates that the dust emission is primarily heated by the AGN.

3.3. *Broadband SEDs for the Different Spatial Components*

To further investigate the dust heated by the AGN (which we refer to as the AGN emission for simplicity), we examine the 3.6–850 μm broadband SEDs. First, it is necessary to separate the emission from the AGN from the various other spatial components in the galaxy, so we first model the 3.6–160 μm images in § 3.3.1. The parameters from the models fit to the data include

flux densities that are then used to construct SEDs. These SEDs are analyzed in § 3.3.2.

3.3.1. *Image Modeling*

The basic image models consists of four parts: an unresolved nuclear point source (from the region heated by the AGN), a dust ring with a radius and radial width described by the Gaussian function $e^{-[(r-r_0)^2/2w^2]}$, an inner dust disk with an exponential profile described as $e^{-r/h}$ that was truncated at the radius of the ring, and a bulge with a simplified de Vaucouleurs profile $e^{-7.67r_{\rm ell}^{0.25}}$, where $r_{\rm ell} = [(x/r_x)^2 + (y/r_y)^2]^{0.5}$ (with r_x and r_y representing the semimajor and semiminor axes of the ellipse that contains half of the total light from the bulge). Each component also has a scaling term that gives the total flux density of the component. These components were convolved to the resolutions of the various *Spitzer* wave bands with PSFs created with STinyTim,[12] a PSF simulator designed for *Spitzer* (Krist 2002). An additional background term was also included in the analysis, although this term was statistically consistent with zero.

To streamline the processing, a few simplifications were made in the modeling. The galaxy center was fixed to match the observed galaxy center. The ratio of the minor and major axes for the disk and the ring were treated as only one free parameter (i.e., the ratios were the same for the ring and disk). The position angle of the major axes for the ring, disk, and bulge components was also treated as only one free parameter. The models were fit only to the region enclosed by the ellipse where the *B*-band surface brightness reaches 25 mag arcsec^{-2}, as defined in the Third Reference Catalogue of Bright Galaxies (de Vaucouleurs et al. 1991). The total of the flux densities for all the components was forced to equal the total flux density within the optical disk. Uncertainties from the fits were generally estimated by the variations in the parameters to fits performed on the north, south, east, or west halves of the optical disk.

Because of variations among the different observations, the fits were customized slightly for each wave band. The customizations are described below:

1. At 3.6–24 μm, matching the exact shape of the PSF of the nucleus became too difficult (mainly because of the limitations of the STinyTim software), so the inner 10″ at 3.6–8 μm and the inner 30″ at 24 μm were not included in the initial fits to the data (although the portion of the PSF that extends outside this region from the nucleus was included). After the models were fit to the data, we used the results to determine the flux densities of the bulge, disk, and ring components within this inner region. These components' flux densities were subtracted from the total flux density within the central region to produce an estimate of the nuclear flux densities that were next aperture-corrected using the PSFs from STinyTim.

2. At 3.6 and 4.5 μm, the ring feature was very faint. If the ring radius and width were allowed to vary as free parameters, the results failed to model either the ring or disk components of the galaxy properly. Therefore, the ring radius and width were fixed to match the parameters from the 5.7−70 μm data, although the ratio of the minor and major axes and the position angle of the major axis were allowed to vary.

3. At 70 and 160 μm, emission from the bulge is no longer discernible in the data. If the bulge is included in the 70 μm model, the resulting bulge parameters are physically implausible results. The bulge is therefore not included in these models. In addition, the value of the residual background term from the fits, which is statistically equal to 0, demonstrates that the bulge component does not need to be included.

4. In the 160 μm fits, the 40″ resolution of the data, as well as the low sampling (where each location is only observed 4 times), make the spatial parameters fit to the data questionable. Therefore, the parameters describing the shapes of the profiles were fixed to values determined from the 5.7−70 μm data, and the fits were performed only to determine the flux densities of the different components. Uncertainties were estimated by examining the change in the fits when the spatial parameters were varied 1 σ.

As an example of the fits, the separate nucleus, inner disk, ring, and bulge components of the model for the 24 μm data are shown in Figure 6. The observed 24 μm image, the model 24 μm image, and the residuals from subtracting the model from the observed image are shown in Figure 7. Note that the structures in the residual basically show substructure in the PSF of the nucleus, which is a manifestation of the limitations of the STiny-Tim software, and substructure in the ring, which is not perfectly described by a Gaussian function and which does contain some bright knots and faint extensions at the east and west ends of the ring that possibly correspond to the faint outer ring described by Bajaja et al. (1984) or faint spiral arm structures. Otherwise, the residual image shows no evidence of any additional structures present in the data.

The parameters that describe the shapes of the model components are presented in Table 2. The weighted mean and standard deviations of the 5.7−70 μm parameters describing the disk and ring (used as described above in the 3.6, 4.5, and 160 μm fits) are described in Table 3. Note that, in the 5.7−70 μm range, the variation in the parameters between wave bands is statistically small. This demonstrates that the shape of the features is relatively invariant across this wavelength range. We can infer that each component can be approximated as uniform in color across this wavelength range, because if color gradients were present, the parameters describing the shapes of the components would vary across different wave bands. For example, if the inner disk had a color gradient, this would manifest itself as a variation in the scale length of the exponential function that
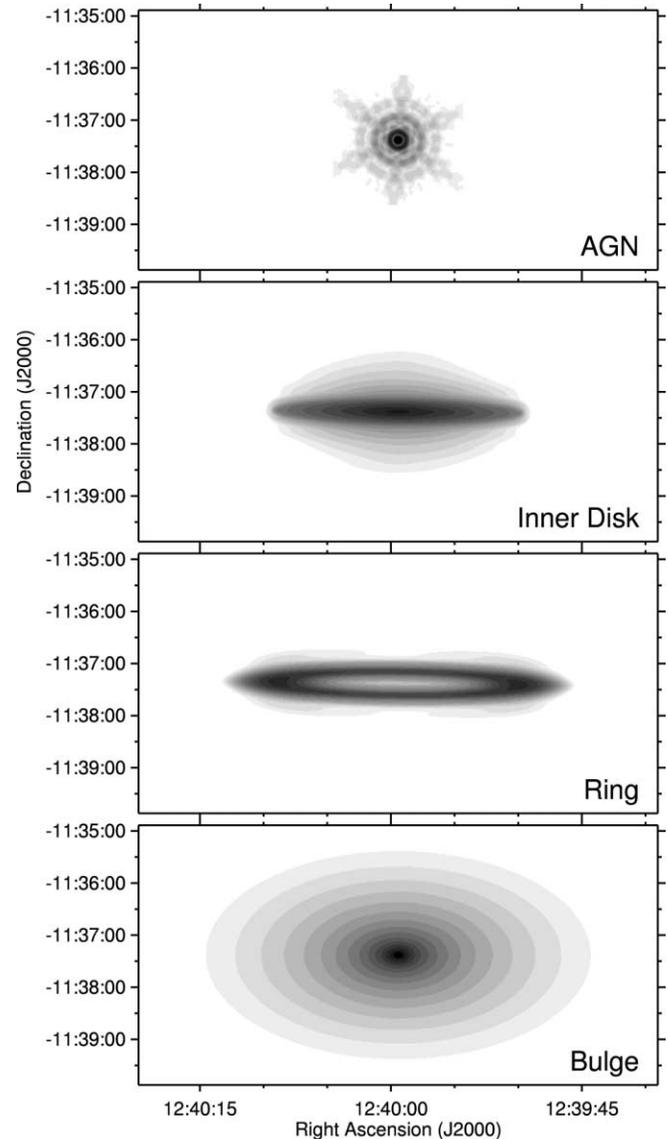

Fig. 6.—Models of the AGN, inner disk, ring, and bulge (all convolved with the 24 μm model PSF) made using the parameters determined from fitting the models to the 24 μm image. This is presented as an example of the image models that were fit to the data. For display purposes, the brightnesses of the model components are not scaled relative to each other. [*See the electronic edition of the Journal for a color version of this figure.*]

describes the inner disk, with some wave bands having a shorter scale length than others. Since no statistical variation in this scale length is present, no color gradient is present.

The flux densities from the fits are given in Table 4. The uncertainties in the tables are from the fits; these uncertainties effectively reflect the contribution of background noise or substructures to the uncertainty. Calibration uncertainties, which are given in the final column of the table, are usually, but not always, higher.

At 850 μm, the emission from outside the nucleus is negligible. No significant structures are visible at above the 3 σ level, although some emission fainter than 3 σ may be associated with the dust ring. As an approximation, however, this source can be treated as a single unresolved source. To obtain a nuclear flux density, we simply measured the emission within the central 1′ of the galaxy. The measured flux density is 0.25 Jy with a calibration uncertainty of 10%. Note that this flux density measurement

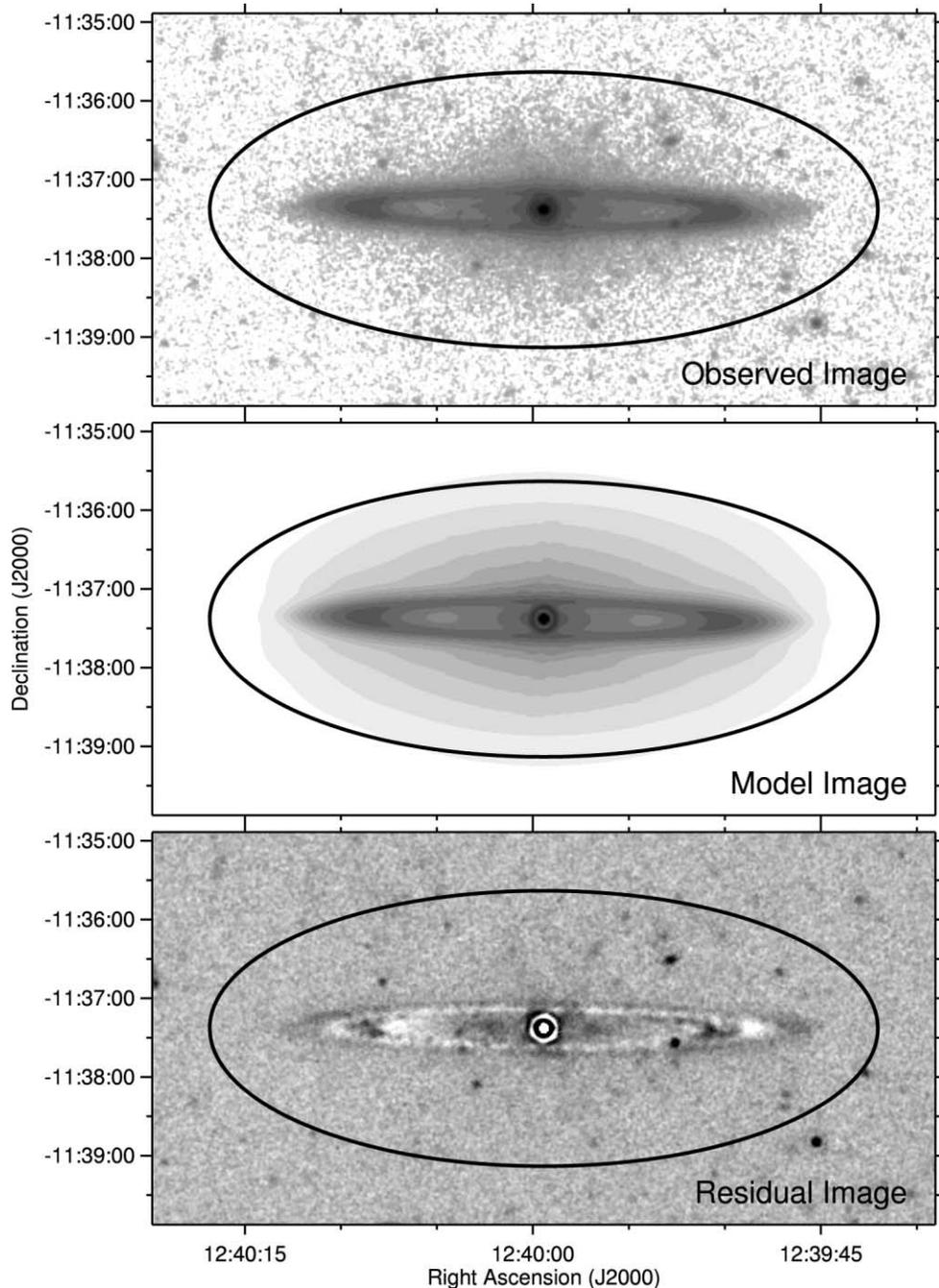FIG. 7.—Observed 24 μm image, the model 24 μm image, and the residuals from subtracting the model from the observed image. This is presented as an example of the image models that were fit to the data. The optical disk of the galaxy (as given by de Vaucouleurs et al. 1991) is overplotted as ovals to show the region over which the fit was performed. [*See the electronic edition of the Journal for a color version of this figure.*]

is consistent with the 870 μm flux density measurement of 0.230 $\pm$ 0.035 Jy measured by Krause et al. (2006). However, we note that some fraction of the flux density within this aperture may originate from the inner disk and ring. We used the parameters given in Tables 3 and 4, as well as the models of the SEDs of each component discussed in § 3.3.2, to construct models of the disk and ring at 850 μm. These models show that 20% or less of the measured 850 μm emission may originate from the inner disk and ring. This estimate, however, relies on an extrapolation of SED models from shorter wavelengths; the 850 μm flux densities of these sources cannot be constrained with these data. (Note that the predicted 850 μm surface brightnesses of the disk and ring are equivalent to the noise levels in the map.) Therefore,

in Table 4 we report the flux density of the nucleus to be 0.25 Jy with an uncertainty of 0.05 Jy (20%).

3.3.2. *Analysis of the SEDs of the Separate Model Components*

The SEDs of the total emission within the optical disk of the galaxy, as well as the SEDs for the nucleus, disk, ring, and bulge components, are presented in Figure 8. For comparison to the SEDs of nearby galaxies, we used the results of fitting semiempirical dust models to the global SEDs of SINGS galaxies in (Dale et al. 2005) to determine what the SED of a typical galaxy was. The median α (the index for the power law that describes the distribution of the intensities of the radiation fields that heat the dust) of the models fit to these galaxies is 2.375. The semiempirical

BENDO ET AL.

TABLE 2
SPATIAL MODEL PARAMETERS OF THE SEPARATE COMPONENTS OF NGC 4594 FROM FITS TO DATA

WAVELENGTH (μm)	DISK/RING/BULGE MAJOR AXIS POSITION ANGLE[a]	DISK/RING MINOR/MAJOR AXIS RATIO	INNER DISK SCALE LENGTH[b]	RING PARAMETERS		BULGE SCALING PARAMETER	
				Radius[b]	Width[b]	Major Axis	Minor Axis
3.6..............	$89°4 \pm 0°4$	0.0996 ± 0.0003	$50''5 \pm 0''5$	[c]	[c]	$141'' \pm 4''$	$78''0 \pm 1''1$
			2.25 ± 0.02 kpc			6.29 ± 0.18 kpc	3.48 ± 0.05 kpc
4.5..............	$89°4 \pm 0°4$	0.1010 ± 0.0018	$51''3 \pm 0''9$	[c]	[c]	$139'' \pm 5''$	$80'' \pm 5''$
			2.29 ± 0.04 kpc			6.2 ± 0.2 kpc	3.6 ± 0.2 kpc
5.7..............	$89°24 \pm 0°03$	0.1026 ± 0.0010	$54'' \pm 3''$	$145''9 \pm 1''.6$	$24''5 \pm 0''3$	$170'' \pm 4''$	$102''5 \pm 1''6$
			2.4 ± 0.13 kpc	6.51 ± 0.07 kpc	1.092 ± 0.013 kpc	7.58 ± 0.18 kpc	4.57 ± 0.07 kpc
8.................	$89°25 \pm 0°14$	0.099 ± 0.003	$46'' \pm 3''$	$144'' \pm 2''$	$21''3 \pm 0''8$	$180'' \pm 9''$	$101''1 \pm 1''2$
			2.05 ± 0.13 kpc	6.42 ± 0.09 kpc	0.95 ± 0.04 kpc	8.0 ± 0.4 kpc	4.5 ± 0.05 kpc
24...............	$89°27 \pm 0°04$	0.0959 ± 0.0009	$45'' \pm 7''$	$144''9 \pm 1''5$	$19''4 \pm 0''5$	$180'' \pm 50''$	$100'' \pm 16''$
			2.0 ± 0.3 kpc	6.46 ± 0.07 kpc	0.87 ± 0.02 kpc	8 ± 2 kpc	4.5 ± 0.7 kpc
70...............	$89°5 \pm 0°3$	0.102 ± 0.005	$39'' \pm 5''$	$143''9 \pm 1''4$	$20''1 \pm 1''6$	. . .	. . .
			1.7 ± 0.2 kpc	6.42 ± 0.06 kpc	0.90 ± 0.07 kpc		

[a] This angle is in degrees east from the north-south axis.
[b] Angular values for these parameters refer to angular distances along the major axis.
[c] Values were fixed to weighted mean values from 5.7–70 μm data given in Table 3.

model with this α is plotted on top of the SEDs in Figure 8 as dotted lines. In addition, emission models comprised of starlight added to the physical dust models of Li & Draine (2001) have been fit to the SEDs of the nucleus, the inner disk, and the ring. The models treat the dust as a mixture of amorphous silicate and carbonaceous grains (including PAHs) with a size distribution that reproduces the optical and ultraviolet extinction in the Milky Way. The dust grains in this model are then heated by starlight with a distribution of intensities given by a power law. In fitting this model to the data, the parameters allowed to vary included the mass of the dust, the index for the power law describing the distribution of intensities of the radiation fields that heat the dust, the maximum and minimum of the radiation fields, the PAH abundance, and the starlight intensity. These models are plotted on top of the SEDs in Figure 8 as solid lines.

The global SED appears similar to the typical SEDs of nearby spiral galaxies (e.g., Regan et al. 2004; Dale et al. 2005). The SEDs of the individual components, however, look very different from each other. In the following paragraphs, the SEDs of the individual components are discussed as they appear in Figure 8, except for the SED of the nucleus, which is discussed last.

The disk 70/160 μm color is relatively warm compared to the ring emission and the total emission, but it is close to the what is expected for the typical galaxy in Dale et al. (2005). The far-

TABLE 3
WEIGHTED MEAN AND STANDARD DEVIATION OF THE MEAN OF DISK AND RING MODEL PARAMETERS FROM 5.7–70 μm DATA

Quantity	Value
Disk/ring major axis position angle[a]............................	$89°25 \pm 0°06$
Disk/ring major/minor axis ratio	0.0990 ± 0.0015
Inner disk scale length[b]	$48'' \pm 3''$
	2.14 ± 0.13 kpc
Ring radius[b]	$144''7 \pm 0''5$
	6.45 ± 0.02 kpc
Ring width[b]..	$22''9 \pm 1''1$
	1.02 ± 0.05 kpc

[a] This angle is in degrees east from the north-south axis.
[b] Angular values for these paramteres refer to angular distances along the major axis.

infrared color temperature (defined in this paper as the temperature of the blackbody function modified by a λ^{-2} emissivity law that fits the 70 and 160 μm data) can be used as an approximation of the dust temperature. In the case of the inner disk, the far-infrared color temperature is 26 ± 2 K. The interstellar radiation field determined from fitting the Li & Draine (2001) model to the data can also be used as an indicator of how much the dust is heated. In the inner disk, the average intensity of the radiation field is approximately 4 times the local value (i.e., the interstellar radiation field near the Sun). The Li & Draine (2001) models also predict that the total dust mass is 3.5×10^5 $M_\odot$. Note that this is a relatively small amount of dust compared to the total dust mass of the ring (given in the next paragraph).

The colors of the dust ring are comparable to the colors of typical nearby galaxies, although the 160 μm emission is slightly higher than what is expected for the typical SED in Dale et al. (2005). The far-infrared color temperature is 19 ± 2 K, and the average intensity of the radiation field determined from the Li & Draine (2001) model fits is equivalent to the local value. The total dust mass predicted for the ring by the model is 7.9×10^6 $M_\odot$. Assuming that the gas-to-dust mass ratio is similar to the value of 165 for the Milky Way (Li 2005), the gas mass as determined from the dust mass is 1.3×10^9 $M_\odot$. For comparison, the atomic gas mass given in Bajaja et al. (1984) is 3.2×10^8 $M_\odot$ (when scaled to a distance of 9.2 Mpc) and the upper limit of the molecular gas mass given in Bajaja et al. (1991) is given as 4.4×10^8 $M_\odot$ (when scaled to a distance of 9.2 Mpc). The upper limit on the total atomic and molecular gas mass is therefore approximately 7.6×10^8 $M_\odot$, which is within a factor of 2 of the gas mass estimate of the dust mass. These results suggest that the majority of the expected mass of dust in this galaxy can be accounted for in the ring.

The SED of the bulge decreases monotonically from short wavelengths to long wavelengths and virtually disappears at 70 μm. The slope of the SED is shallower than what is expected from blackbody emission, possibly hinting at the presence of hot dust in the atmospheres of evolved stars in the bulge (see Bressan et al. 1998, for example). At 8 μm, half of the global flux from NGC 4594 originates from the bulge, and at 24 μm, the bulge still contributes one-third of the total flux.

Of most interest, however, is the unusual SED of the nucleus. Note the relatively hot colors compared to the ring and disk. The

TABLE 4
FLUX DENSITY MODEL PARAMETERS OF THE SEPARATE COMPONENTS OF NGC 4594

WAVELENGTH (μm)	FLUX DENSITY (Jy)[a]					CALIBRATION UNCERTAINTY (%)
	Global	Nucleus	Inner Disk	Ring	Bulge	
3.6	3.50	0.0847 ± 0.0008	0.529 ± 0.006	0.168 ± 0.011	2.684 ± 0.017	30
4.5	2.09	0.0614 ± 0.0008	0.309 ± 0.009	0.111 ± 0.003	1.595 ± 0.016	30
5.7	2.01	0.0473 ± 0.0003	0.265 ± 0.006	0.199 ± 0.004	1.496 ± 0.003	30
8	1.64	0.0344 ± 0.0009	0.156 ± 0.009	0.482 ± 0.008	0.96 ± 0.02	30
24	0.65	0.061 ± 0.006	0.062 ± 0.014	0.277 ± 0.006	0.25 ± 0.03	10
70	6.7	0.203 ± 0.018	1.9 ± 0.2	4.6 ± 0.2	. . .	20
160	35.1	0.33 ± 0.05	2.8 ± 0.2	32.0 ± 0.2	. . .	20
850	. . .	0.25 ± 0.05	. . .	. . .	. . .	10

[a] The uncertainties in these columns are from the fits to the data and do not include the calibration uncertainties. The calibration uncertainties are listed in the final column.

24/70 and 24/160 μm colors are relatively high. The far-infrared color temperature is 25 ± 2 K, and according to the Li & Draine (2001) dust model fit to the data, the average radiation field in the nucleus is approximately 6 times the local value. Strangely, the 70–850 μm emission almost appears to be flat, in contrast to the ring and inner disk SEDs. Of particular interest is the 160 and 850 μm emission. Placed in the context of the SEDs of other nearby galaxies, the 70 μm emission and especially the 160 μm emission is relatively weak compared to emission at 24 μm and shorter wavelengths. The 850 μm emission is of interest in that it is abnormally high compared to the 70 and 160 μm data, and it cannot be reproduced by the Li & Draine (2001) dust model fits.

Note that the nuclear emission represents the enhancement of emission by the AGN itself. As demonstrated in § 3.2, star formation is either absent from the nucleus or makes only a negligible contribution to the radiation field in the center of the galaxy. Passive heating from evolved stars in the inner disk or the bulge is another possibility. However, note that the scale lengths of the inner disk and the bulge do not vary between 5.7 and 70 μm. This indicates that the infrared colors of the bulge and disk do not vary and that the nuclear emission is not the result of an enhancement in the nuclear infrared colors from evolved stars. The nuclear infrared emission must be enhanced by the AGN.

4. DISCUSSION

The 24–850 μm regime of the nuclear SED leads to two significant results. The first result is the especially low 160 μm emission from the nuclear region (compared to emission at 24 μm and shorter wavelengths) and its possible connection to the weak circumnuclear star formation activity (as revealed by the absence of PAH emission). The other result is the unusually high 850 μm emission, which appears to originate from a source other than the ∼20–30 K dust typically found in the interstellar medium of other galaxies or in the ring and inner disk of this galaxy. We discuss these two results below.

4.1. *The Implications of the Weak Nuclear* 160 *μm Emission*

The weak 160 μm emission from large, cool grains in the environment around this AGN is best understood when placed in the context of the relation between far-infrared emission and either AGN or star formation activity in other AGN host galaxies. Early results from *IRAS*, such as Rodriguez Espinosa et al. (1987) and Rowan-Robinson & Crawford (1989), had suggested that far-infrared emission from nearby Seyfert galaxies was associated with star formation, not AGN activity. In later studies of Seyfert galaxies, including Maiolino et al. (1995), Rodriguez Espinosa & Perez Garcia (1997), and Perez Garcia et al. (1998, 2000), the far-infrared dust emission, while still observed to be strongly peaked near the centers of the galaxies, had been shown to be associated with star formation, and the contribution of dust heated by the AGN to the nuclear emission was minimal.

In contrast to the observations of Seyfert galaxies cited above, the 160 μm emission commonly associated with star formation
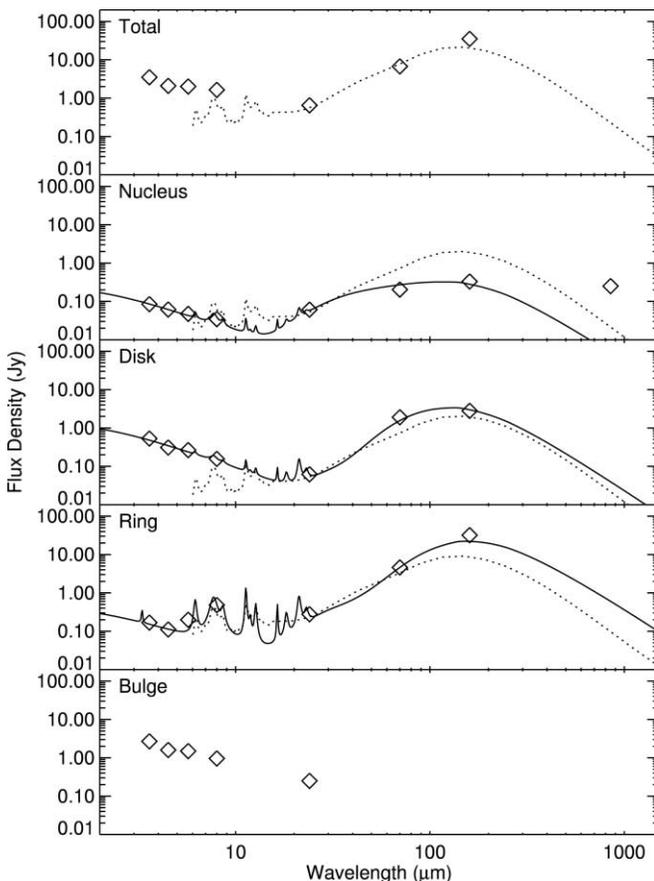

FIG. 8.—SEDs of the separate components of NGC 4594. The error bars are equal to or smaller than the size of the plot symbols. For comparison between the SEDs, the y-axes of all the plots are fixed to the same scale. For comparison to the SEDs of nearby galaxies, the semiempirical dust model from Dale et al. (2005) with a median α-value (explained in the text) is plotted over the total, nucleus, disk, and ring SEDs as a dotted line. This semiempirical model has been scaled to match the 24 μm flux density in each SED. Emission models comprised of starlight added to the Li & Draine (2001) dust models are included in the plots of the nucleus, disk, and ring SEDs.

or cirrus emission does not peak in the center of NGC 4594. PAH emission is also largely absent from inside the ring, which is consistent with the AGN being the dominant energy source in this region. The molecular gas that is associated with star formation seems to be limited to the dust ring. CO data presented in Bajaja et al. (1991) show that the CO emission detected from the galaxy corresponds to only locations in the dust ring, not the nucleus. CO observations in Young et al. (1995) show that the molecular gas is uniformly distributed along the major axis, which implies that it corresponds best to the dust emission from the ring (although note that the individual pointings only detect CO at the 2 σ level). The interstellar gas around the AGN appears to be predominantly hot X-ray-emitting gas (Pellegrini et al. 2002), which cannot fuel star formation and which may be too low in density to fuel enhanced AGN activity.

The differences between NGC 4594 and Seyfert galaxies in terms of circumnuclear far-infrared emission therefore appears to be connected to circumnuclear star formation activity. In Seyfert galaxies, star formation and the far-infrared dust emission associated with it are typically found near the AGN. The presence of strong star formation (or relatively young stellar systems) near Seyfert nuclei has been noted previously (Gonzalez-Delgado & Perez 1993; Maiolino et al. 1995; Oliva et al. 1995, 1999; Heckman et al. 1997; González Delgado et al. 1998, 2001), although the observations have generally found the presence of strong circumnuclear star formation in Seyfert 2 galaxies rather than Seyfert 1 galaxies. In the case of the AGN in NGC 4594, however, the cool gas that fuels both enhanced star formation and AGN activity is not present. Therefore, the region is devoid of the long-wavelength far-infrared emission from the ~20 K dust associated with molecular gas.

The absence of recent star formation is observed in at least a significant fraction of nearby LINER and low-luminosity AGN nuclei (Larkin et al. 1998; Cid Fernandes et al. 2004; Gonzáles Delgado et al. 2004; Bendo & Joseph 2004) and the relative lack of mid-infrared dust emission in LINERs compared to other galaxies (Bendo et al. 2002) has been observed before. The data taken for all SINGS galaxies, as well as other mid- and far-infrared surveys of nearby LINERs and low-luminosity AGNs, should be used to determine whether AGN nuclei like NGC 4594 are also weak yet hot infrared sources.

4.2. The Origin of the 850 μm Emission

In most galaxies, the 850 μm wave band is dominated by ~20–30 K dust emission (e.g., Dunne et al. 2000; Dunne & Eales 2001; Bendo et al. 2003; Regan et al. 2004). In NGC 4594, however, the difference in morphology between the 160 and 850 μm images, as well as the relatively high ratio of 850 to 160 μm flux densities for the nucleus, clearly demonstrate that the 850 μm emission is not from ~20–30 K dust. The 850 μm emission must originate from another source, possibly one connected to the high-energy phenomena observed in other wave bands. We examine a number of alternative 850 μm emission mechanisms below.

4.2.1. Very Cold Dust or Exotic Dust Emission

When excess emission is observed at submillimeter wavelengths compared to the modified blackbody emission at far-infrared wavelengths, one common explanation is that the excess emission comes from very cold dust at temperatures in the 5–10 K range. Therefore, we consider whether the excess submillimeter emission from the nucleus of NGC 4594 is from such dust emission.

Qualitatively, it seems unlikely that a very cold dust component could be responsible for the excess emission seen at 850 μm.

First, Figures 1 and 8 show that the dust in the nucleus is strongly heated by the AGN. The high temperatures of the circumnuclear environment are also evident in the Hα emission (Ho et al. 1997), which demonstrate that photoionizing photons are present, and in the X-ray observations (Pellegrini et al. 2002, 2003), which demonstrate that both hot X-ray gas and hard X-ray synchrotron emission is present. For a large mass of very cold dust to exist in such an environment seems unlikely. Furthermore, to have a significant very cold dust component present without any strong emission from a ~20–30 K dust component seems unlikely.

To examine this further, we calculated the minimum dust mass that would be needed to produce the 850 μm emission using the equation

$$M_{\text{dust}} = \frac{D^2 f_{850\,\mu m}}{\kappa_{850\,\mu m} B(T)_{850\,\mu m}}, \qquad (1)$$

where D is the distance to the object (9.2 Mpc), $f_{850\,\mu m}$ is the 850 μm flux density, $\kappa_{850\,\mu m}$ represents the absorption opacity of the dust at 850 μm (0.431 cm^2 g^{-1}; Li & Draine 2001), and $B(T)_{850\,\mu m}$ is the surface brightness of a pure blackbody at a temperature T. The minimum dust mass will correspond to the warmest temperature that is still consistent with the data. This temperature will describe the modified blackbody function that fits both the 160 and 850 μm measurements. Using an emissivity varying as λ^{-2} (which approximates the emissivity of dust in the far-infrared and submillimeter; see Li & Draine 2001), the modified blackbody that best fits the 160 and 850 μm data has a temperature of 9 ± 2 K. This is consistent with a dust mass of $1.9 \times 10^7 M_\odot$. Note, however, that a substantial part of the 160 μm emission probably comes from warmer dust emission, as would be implied from the emission at 70 μm (see, e.g., the model fit to the nuclear SED in Fig. 8). The temperature of this hypothetical very cold component could be lower, which would drive the dust mass of the very cold component higher.

Assuming a gas-to-dust mass ratio of 165, the minimum dust mass calculated above implies a total gas mass of $3.2 \times 10^9 M_\odot$ in the central 15″ region of the galaxy (or within a radius of 330 pc of the center). This gas mass is higher than the upper limit of $7.8 \times 10^8 M_\odot$ for the global total of atomic and molecular gas in NGC 4594 (as calculated in § 3.3.2), so it is implausible to expect so much gas to be present in the center. Furthermore, the black hole in the AGN itself is $10^9 M_\odot$. It is implausible to think that a mass of cold gas multiple times larger than the mass of the central AGN could be located in an environment where significant numbers of high-energy photons from the AGN and hot gas are present (e.g., Pellegrini et al. 2002, 2003). Even if only half the submillimeter emission originates from ~10 K dust, the implied molecular gas mass is still larger than the mass of the black hole. Therefore, we reject the possibility that a very cold dust component is generating the 850 μm emission.

Another possibility is that the submillimeter emission might be produced by grains with a much larger submillimeter opacity than the grains that appear to be responsible for the bulk of the far-infrared and submillimeter emission observed from most galaxies. Exotic grains such as fractal grains have been proposed as an explanation for the excess submillimeter emission observed from objects such as the Milky Way (Reach et al. 1995) and NGC 4631 (Dumke et al. 2004). Such dust would have temperatures of 5–10 K and would radiate predominantly at submillimeter wavelengths.

This explanation, however, has problems. Even if the exotic grains have a sufficiently high ratio of submillimeter opacity to optical-ultraviolet opacity to remain at ~10 K in the intense

radiation field, the required dust mass would remain unacceptably large unless the grains have a submillimeter opacity orders of magnitude larger than normal dust. While very large submillimeter opacities have been reported for some laboratory materials (e.g., material "BE" of Mennella et al. 1998), no evidence suggests that such materials exist in interstellar space (e.g., B. T. Draine 2006, in preparation).

4.2.2. CO *Emission*

The contribution of CO (3–2) emission to broadband 850 μm emission has been a concern when using these wave bands for measurements of dust SEDs in the 15–30 K range. Usually, CO (3–2) emission is only a minor contribution to the total submillimeter emission, although some exceptional cases have been identified (e.g., Klaas et al. 2001).

Bajaja et al. (1991) detected the CO (1–0) line 140″ east and west of the nucleus in NGC 4594 but did not detect the central position because of instrumental problems. The data in (Young et al. 1995) show that the CO (1–0) emission does not peak in the center of the galaxy but is instead uniformly distributed along the major axis (although note that CO is detected in the individual pointings at only the 2 σ level). Qualitatively, these data suggest that the CO (1–0) emission is primarily in the dust ring, not in the nucleus.

To estimate the possible 850 μm flux density of the CO (3–2) line in the nucleus, we use the (Young et al. 1995) CO (1–0) upper limit of 1.6 K km s^{-1} for the center of NGC 4594. Using the conversion factor of 42 Jy K^{-1} from Young et al. and the assumed line width of 400 km s^{-1}, the upper limit of the flux density of the CO (1–0) transition is ~0.017 Jy. Assuming that the CO J levels are thermalized at a rotational temperature $T_{rot} > 15$ K, we estimate an upper limit for the flux density of ~1.5 Jy for the CO (3–2) transition. Using the relative width of the potential line (~400 km s^{-1}) and the SCUBA 850W filter bandpass (40 GHz), we obtain an upper limit for the contribution of the CO flux density at 850 μm of ~20 mJy, which is much less than the 250 mJy measured for the nucleus. We therefore conclude that emission from CO cannot explain all of the emission at 850 μm.

4.2.3. *Synchrotron Emission*

Synchrotron emission has been observed at submillimeter wavelengths in such AGNs as NGC 4374 (Leeuw et al. 2000) and NGC 1275 (Irwin et al. 2001). Therefore, it is a natural possibility as the source of the submillimeter emission in this galaxy.

To determine the contribution of synchrotron emission at 850 μm, we extrapolate from radio observations to the submillimeter. The best published multiwavelength radio data taken for this galaxy come from de Bruyn et al. (1976) and Hummel et al. (1984). Their results show that all of the radio emission from NGC 4594 originates from the AGN, which appears as an unresolved source. The SED shows that the radio emission consists of synchrotron emission with a break at approximately 6 cm (5 GHz) caused by synchrotron self-absorption. A power-law fit to the 2–6 cm (15.0–5.0 GHz) data from Hummel et al. (1984) shows that flux density is proportional to $\lambda^{0.2}$. Using this power-law fit to extrapolate from centimeter to submillimeter wavelengths as shown in Figure 9, we predict an 850 μm flux density of 0.056 Jy, which is approximately a factor of 4 lower than the measured flux density.

Variable submillimeter synchrotron emission is a possibility. The synchrotron emission from the AGN is variable, but the variability may not be significant enough to explain the difference between the observed 850 μm flux density and the extrapolations of synchrotron emission to those wavelengths. Decades of observations show that the 6 cm radio emission has only been
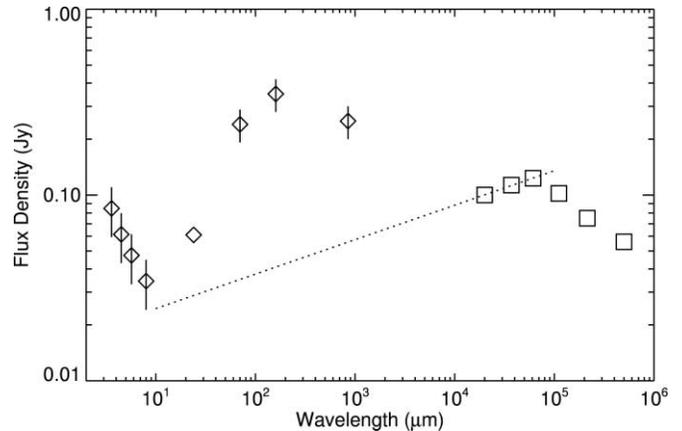

Fig. 9.—Observed SED of the AGN of NGC 4594 (*diamonds*), along with the radio observations by Hummel et al. (1984; *squares*) and the power law for the synchrotron emission as inferred from the radio data (*dotted line*). Except where shown, the error bars are equal to or smaller than the size of the plot symbols. Note that the extrapolations fall short of the measured 850 μm flux density. See the text for a discussion of radio observations other than those in Hummel et al. (1984).

observed to vary at the 10%– 20% level (de Bruyn et al. 1976; Ekers et al. 1983; Krause et al. 2006). Bajaja et al. (1988) and references therein found that the 20 cm flux density increased by ~70% between 1980 and 1985. However, this increase was not observed at other wavelengths, nor is it clear that this variability is seen at other wavelengths. At 3.6 cm, Thean et al. (2000) measured a flux density of 84.7 ± 0.05 mJy in 1995–1996, and Krause et al. (2006) measured a flux density of 90 ± 10 mJy in 2003. These values are lower than the 113 ± 12 mJy measured by de Bruyn et al. (1976). However, it is unclear whether this represents a decrease in the luminosity of the source itself or an improvement in the calibration of measurements at these wavelengths. Moreover, this decrease is unlikely to correspond to an increase in synchrotron emission at 850 μm unless the power law describing the synchrotron emission changes as well. Finally, we would like to state that the consistency between the 850 μm flux density measured in this paper and the 870 μm flux density measured in Krause et al. (2006) implies that the submillimeter emission is not variable at a level greater than the measurement uncertainties (10%), at least on periods of ~3 yr. Therefore, it is unlikely that the submillimeter emission observed at 850 μm was captured at a maximum in emission while the radio emission was taken at a minimum.

Nonetheless, we are still hesitant to rule out synchrotron emission entirely as a source of the 850 μm emission. The extrapolation from radio wavelengths did yield an estimate of the 850 μm emission that was within less than a factor of 10 of the measured flux density. The power law used in the extrapolation was determined using only three data points, and the extrapolation extended over a factor of 10 in wavelength. So, we caution that the extrapolations are not entirely reliable and that the actual synchrotron emission may be higher or lower than what we determined here.

It is also possible that the 850 μm emission is from synchrotron emission unrelated to the centimeter wavelength emission. Such synchrotron emission would need to be self-absorbed at wavelengths longer than 850 μm. To determine whether such a synchrotron component is present would require further observations in multiple wave bands between 350 μm and 2 cm.

4.2.4. *Bremsstrahlung*

A final possibility is that bremsstrahlung emission is responsible for the 850 μm emission. Bremsstrahlung emission has been

detected in some nearby objects, such as M82 (e.g., Condon 1992), but has never been identified as a dominant source at 850 μm.

Since bremsstrahlung emission and recombination line emission both originate from ionized hydrogen gas, it is possible to relate the two emission processes to infer the expected bremsstrahlung emission. To convert the Hα flux to 850 μm flux density, we use the equations from Appendix A in Caplan & Deharveng (1986). We assume that the temperature is $\sim 10^4$ K and the contribution of He II to the bremsstrahlung emission is negligible. This gives the conversion

$$f_\nu(850\,\mu\text{m};\text{Jy}) = 5.29 \times 10^9 f(\text{H}\alpha;\ \text{ergs cm}^{-2}\ \text{s}^{-1}). \quad (2)$$

Ho et al. (1997) give the Hα flux as measured in a $2''$ wide region as 1.05×10^{-13} ergs cm^{-2} s^{-1}. This yields an expected 850 μm bremsstrahlung flux density of 5.5×10^{-4} Jy. This is a factor of 400 too low to explain the observed 850 μm flux density from the AGN. Note that the Ho et al. measurements are not corrected for dust extinction. However, the low extinction measured with the Hα/Hβ ratio in Ho et al. implies that the extinction correction for the Hα flux would not significantly change the estimate of the 850 μm bremsstrahlung emission. Therefore, we conclude that some other emission process must be responsible.

4.2.5. Conclusions on the Origin of the 850 μm Emission

This analysis has shown that no known emission mechanism can satisfactorily explain the observed 850 μm flux density of 0.25 Jy from the nucleus of NGC 4594. Synchrotron emission seemed to be the most plausible single mechanism to explain the 850 μm emission, although the 0.056 Jy flux density at 850 μm inferred from the radio synchrotron emission falls short of the observed flux density. However, it still possible that this synchrotron emission contributes a fraction of the total 850 μm flux density. CO emission, with a flux density of 0.020 Jy, and bremsstrahlung emission, with a flux density of 5.5×10^{-4} Jy, are also physically plausible emission mechanisms that may contribute to the 850 μm band. Very cold dust (at temperatures of ~ 10 K) is not a physically plausible source of 850 μm emission, although some small amount of the flux density (approximately 2% according to the Li & Draine [2001] dust models fit to the nuclear SED in § 3.3.2) may be dust emission from warmer dust.

Even though multiple emission mechanisms may contribute to the total nuclear emission at 850 μm, the total flux density of ~ 0.080 Jy from all known physically plausible emission mechanisms (synchrotron, CO, bremsstrahlung, and warm dust emission) still falls short of the 0.250 Jy flux density observed at 850 μm. The possibility remains that some mechanism that is dissociated from the emission mechanisms observed in all other wave bands, such as synchrotron emission that is self-absorbed longward of 850 μm or unidentified spectral line emission, could be responsible for a significant fraction of the 850 μm nuclear emission. Additional submillimeter and millimeter photometry

and spectroscopy are needed to identify the source of the 850 μm emission, which should provide further clues about the nature of this and other similar massive AGNs.

5. CONCLUSIONS

We have extracted the SEDs of the nucleus, inner disk, ring, and bulge in the Sombrero Galaxy, NGC 4594. The SED of the nucleus is notably unusual in that the emission spectrum requires the dust to be hot, that the 160 μm emission is notably weak compared to emission at 24 μm and shorter wavelengths, and that some source other than large ~ 20–30 K dust grains powers the 850 μm emission.

The relatively weak 160 μm nuclear emission appears to indicate that the LINER activity seen in this galaxy is a result of the lack of cool gas needed to fuel stronger Seyfert activity. The corresponding lack of star formation implied by the data is in line with previous studies, which have found weak nuclear star formation activity in many (but not all) LINERs and low-luminosity AGNs. Moreover, the strong far-infrared dust emission from the ISM near Seyfert nuclei, as well as the strong circumnuclear star formation in Seyfert galaxies, also provides credence to this idea.

The abnormally high 850 μm emission from the nuclear region cannot be explained as any kind of dust emission, as synchrotron emission related to that seen at centimeter wavelengths, or as bremsstrahlung emission. A combination of mechanisms may be necessary to explain the 850 μm emission. It is possible that the 850 μm emission may come from an emission source that cannot be inferred from observations in other wave bands, such as synchrotron emission that is self-absorbed at wavelengths longer than 850 μm or unidentified spectral line emission in the 850 μm band. Further observations at submillimeter and millimeter wavelengths are needed to determine the nature of the emission.

Future observations of low-luminosity AGNs with the *Spitzer Space Telescope* may reveal more galaxies with similarly weak nuclear 160 μm emission. Already, SINGS observations of the low-luminosity AGN NGC 2841 indicate that it may have a similar SED. Such anomalous nuclear emission should be placed into context by comparing these sources to similar LINERs and to Seyfert galaxies. The end result may be the identification of key differences between these two classes of objects. We also anticipate that a comparison of 160 μm *Spitzer* images with $15''$ resolution submillimeter or millimeter data will reveal other galaxies with anomalously high submillimeter or millimeter emission, which should lead to identification of the source of the emission and a more complete view of the energetics of AGNs.

REFERENCES

Ajhar, E. A., Tonry, J. L., Blakeslee, J. P., Dressler, A., Holtzman, J. A., & Postman, M. 1997, AJ, 114, 626
Bajaja, E., Dettmar, R.-J., Hummel, E., & Wielebinski, R. 1988, A&A, 202, 35
Bajaja, E., Krause, M., Dettmar, R.-J., & Wielebinski, R. 1991, A&A, 241, 411
Bajaja. E., van der Burg, G., Faber, S. M., Gallagher, J. S., Knapp, G. R., & Shane, W. W. 1984, A&A, 141, 309
Bendo, G. J., & Joseph, R. D. 2004, AJ, 127, 3338
Bendo, G. J., et al. 2002, AJ, 124, 1380
Bendo, G. J., et al. 2003, AJ, 125, 2361
Bressan, A., Granato, G. L., & Silva, L. 1998, A&A, 332, 135
Caplan, J., & Deharveng, L. 1986, A&A, 155, 297
Cid Fernandes, R., et al. 2004, ApJ, 605, 105
Condon, J. J. 1992, ARA&A, 30, 575
Dale, D. A., et al. 2005, ApJ, 633, 857
———. 2006, preprint (astro-ph/0604007)
de Bruyn, A. G., Crane, P. C., Price, R. M., & Carlson, J. B. 1976, A&A, 46, 243

de Grijp, M. H. K., Miley, G. K., Lub, J., & de Jong, T. 1985, Nature, 314, 240
———. 1987, A&AS, 70, 95
de Vaucouleurs, G., de Vaucouleurs, A., Corwin, H. G., Buta, R. J., Paturel, G., & Fouqué, P. 1991, Third Reference Catalogue of Bright Galaxies (Berlin: Springer)
Dumke, M., Krause, M., & Wielebinski, R. 2004, A&A, 414, 475
Dunne, L., & Eales, S. A. 2001, MNRAS, 327, 697
Dunne, L., Eales, S., Edmunds, M., Ivison, R., Alexander, P., & Clements, D. L. 2000, MNRAS, 315, 115
Ekers, R. D., Fanti, R., & Miley, G. K. 1983, A&A, 120, 297
Engelbracht, C. W., Gordon, K. D., Rieke, G. H., Werner, M. W., Dale, D. A., & Latter, W. B. 2005, ApJ, 628, L29
Fazio, G. G., et al. 2004, ApJS, 154, 10
Ford, H. C., Hui, X., Ciardullo, R., Jacoby, G. H., & Freeman, K. C. 1996, ApJ, 458, 455
Genzel, R., & Cesarsky, C. J. 2000, ARA&A, 38, 761
Genzel, R., et al. 1998, ApJ, 498, 579
Gonzáles Delgado, R. M., Cid Fernandez, R., Pérez, E., Martins, L. P., Storchi-Bergmann, T., Schmitt, H., Heckman, T., & Leitherer, C. 2004, ApJ, 605, 127
González Delgado, R. M., Heckman, T., & Leitherer, C. 2001, ApJ, 546, 845
González Delgado, R. M., Heckman, T., Leitherer, C., Meurer, G., Krolik, J., Wilson, A. S., Kinney, A., & Koratkar, A. 1998, ApJ, 505, 174
Gonzalez-Delgado, R. M., & Perez, E. 1993, Ap&SS, 205, 127
Gordon, K. D., et al. 2005, PASP, 117, 503
Heckman, T. M., Gonzalez-Delgado, R., Leitherer, C. Meurer, G. R., Krolik, J., Wilson, A. S., Koratkar, A., & Kinney, A. 1997, ApJ, 482, 114
Helou, G., Lu, N. Y., Werner, M. W., Malhotra, S., & Silbermann, N. 2000, ApJ, 532, L21
Ho, L. C., Filippenko, A. V., & Sargent, W. L. W. 1997, ApJS, 112, 315
Holland, W. S., et al. 1999, MNRAS, 303, 659
Houck, J. R., et al. 2004, ApJS, 154, 18
Hummel, E., van der Hulst, J. M., & Dickey, J. M. 1984, A&A, 134, 207
Irwin, J. A., Stil, J. M., & Bridges, T. J. 2001, MNRAS, 328, 359
Jenness, T., & Lightfoot, J. F. 1998, in ASP Conf. Ser. 145, Astronomical Data Analysis Software and Systems VII, ed. R. Albrecht, R. N. Hook, & H. A. Bushouse (San Francisco: ASP), 216
Kailey, W. F., & Lebofsky, M. J. 1988, ApJ, 326, 653
Kennicutt, R. C., Jr., et al. 2003, PASP, 115, 928
Klaas, U., et al. 2001, A&A, 379, 823

Kormendy, J., et al. 1996, ApJ, 473, L91
Krause, M., Wielebinski, R., & Dumke, M. 2006, A&A, 448, 133
Krist, J. 2002, Tiny Tim/SIRTF User's Guide (Pasadena: SSC)
Larkin, J. E., Armus, L., Knop, R. A., Soifer, B. T., & Matthews, K. 1998, ApJS, 114, 59
Leeuw, L. L., Sansom, A. E., & Robson, E. I. 2000, MNRAS, 311, 683
Li, A. 2005, in Penetrating Bars through Masks of Cosmic Dust, ed. D. L. Block et al. (Dordrecht: Springer), 535
Li, A., & Draine, B. T. 2001, ApJ, 554, 778
Lu, N., et al. 2003, ApJ, 588, 199
Madden, S. C., Galliano, F., Jones, A. P., & Sauvage, M. 2006, A&A, 446, 877
Maiolino, R., Ruiz, M., Rieke, G. H., & Keller, L. D. 1995, ApJ, 446, 561
Mennella, V, Brucato, J. R., Colangeli, L., Palumbo, P., Rotundi, A., & Bussoletti, E. 1998, ApJ, 496, 1058
Oliva, E., Origlia, L., Maiolino, R., & Moorwood, A. F. M. 1995, A&A, 301, 55
———. 1999, A&A, 350, 9
Osterbrock, D. E., & de Roberts, M. M. 1985, PASP, 97, 1129
Peeters, E., Spoon, H. W. W., & Tielens, A. G. G. M. 2004, ApJ, 613, 986
Pellegrini, S., Baldi, A., Fabbiano, G., & Kim, D.-W. 2003, ApJ, 597, 175
Pellegrini, S., Fabbiano, G., Fiore, F., Trinchieri, G., & Antonelli, A. 2002, A&A, 383, 1
Perez Garcia, A. M., Rodriguez Espinosa, J. M., & Fuensalida, J. J. 2000, ApJ, 529, 875
Perez Garcia, A. M., Rodriguez Espinosa, J. M., & Santolaya Rey, A. E. 1998, ApJ, 500, 685
Reach, W. T., et al. 1995, ApJ, 451, 188
Regan, M. W., et al. 2004, ApJS, 154, 204
Rice, W., Lonsdale, C. J., Soifer, B. T., Neugebauer, G., Kopan, E. L., Lloyd, L. A., De Jong, T., & Habing, H. J. 1988, ApJS, 68, 91
Rieke, G. H., et al. 2004, ApJS, 154, 25
Rodriguez Espinosa, J. M., & Perez Garcia, A. M. 1997, ApJ, 487, L33
Rodriguez Espinosa, J. M., Rudy, R. J., & Jones, B. 1987, ApJ, 312, 555
Rowan-Robinson, M., & Crawford, J. 1989, MNRAS, 238, 523
Schmitt, H. R., Kinney, A. L., Calzetti, D., & Storchi Bergmann, T. 1997, AJ, 114, 592
Thean, A., Pedlar, A., Kukula, M. J., Baum, S. A., & O'Dea, C. P. 2000, MNRAS, 314, 573
Werner, M. W., et al. 2004, ApJS, 154, 1
Young, J. S., et al. 1995, ApJS, 98, 219